X-Ray Residual Stress Gradient Analysis in Annealed Silver Thin Films Using Asymmetric Bragg Diffraction

Anouar Njeh[a], Dieter Schneider[b], Hartmut Fuess[c], and Mohamed Hédi Ben Ghozlen[a]

[a] Laboratoire de Physique des Matériaux, Faculté des Sciences, Sfax University, 3018 Sfax, Tunisia
[b] Fraunhofer-Institut für Material- und Strahltechnologie, Winterbergstraße 28, D-01277 Dresden, Germany
[c] Institute of Materials Science, University of Technology, Petersenstraße 23, D-64287 Darmstadt, Germany

Reprint requests to Dr. A. N.; Fax: +216-74-243542; E-mail: njehanouar@yahoo.fr

Z. Naturforsch. **64a,** 112 – 122 (2009); received June 18, 2008

Residual stresses were determined in magnetron-sputtered Ag thin films of 400 nm thickness by asymmetric Bragg scattering. The corresponding $\cos^2\alpha\sin^2\psi$ plots were nonlinear which indicates a strong residual gradient along the depth of the samples. The in-plane stress was highly compressive at the sample surface and became tensile at the interface. The out-plane stress was compressive and reached its maximum at the sample interface. The stress gradient changed significantly with post-annealing temperature. A Young's modulus of $E = 83$ GPa and a Poisson ratio of $\nu = 0.3$ were measured by surface acoustic wave dispersion.

Key words: Residual Stress Gradient; Thin Films; X-Ray Scattering; Surface Acoustic Wave; Grazing Incidence Diffraction.

1. Introduction

The mechanical behaviour and adhesion between coating and substrate are strongly affected by residual stresses. These are inevitably produced in a thin film due to the structural and thermal misfit between the film and substrate [1]. These stresses are often higher than the typical stresses developed in bulk metals, and can produce serious reliability problems.

During the film deposition at elevated temperature or during a thermal treatment process residual strain will build up. Commonly, for thin films four types of stresses are mentioned. Epitaxial stresses (σ_{ep}) arise from the lattice constant mismatch between the lattices of the film and of the substrate. Intrinsic or growth stresses (σ_{in}) result from the deposition process. If the system film/substrate is subjected to a temperature change, then the different thermal expansion coefficients of the film and the substrate will result in thermal stresses (σ_{th}) both in film and substrate. Transformation stresses (σ_{tr}) arise during solid phase transition phenomena.

Many experimental techniques have been developed to measure the amount of stress and strain in thin films. The two general classes of commonly used techniques include deflection techniques based on determining the radius of curvature of the substrate [2], and strain measurement techniques, based on direct measurements of interplanar spacings in the film using X-ray diffraction [3].

Several X-ray diffraction methods have been applied to perform residual stress evaluations (RSEs) within thin films. The most frequent among them are the $\sin^2\psi$ technique [4 – 6], grazing incidence X-ray diffraction (GIXD) [7], grazing exit X-ray diffraction [8], and high-resolution X-ray scattering (HRXRD) [9].

The $\sin^2\psi$ method is based on the shift of a diffraction peak position recorded for different specimen tilt angles ψ, where ψ is the angle between the diffracting plane normal and the specimen surface normal [6]. Usually, the $\sin^2\psi$ method is carried out using a diffractometer which is set up in the Bragg-Brentano geometry (BBG). RSE by GIXD has been described by several authors [10 – 14]. Recognizing the advantages of the $\sin^2\psi$ method and the GIXD techniques a fixed (*hkl*) peak is measured for different ψ tilt under grazing incidence. Such an experimental setup is called asymmetric Bragg diffraction geometry (ABG) [15].

In this paper, we present experimental measurements carried out in ABG to assess the stress-depth

0932–0784 / 09 / 0100–0112 $ 06.00

dependence and the effect of annealing treatment on pure polycrystalline silver films on a silicon substrate.

2. Principles of X-Ray Residual Stress Measurements

2.1. Theoretical Background

The ABG is as follows: the grazing angle γ is defined by the incident X-ray beam and the sample surface angle axis S_1. S_i (i = 1, 2 and 3) are the axes of the sample system **S**. Usually, S_1 and S_2 are contained in the sample surface, and S_3 is chosen perpendicular to the sample surface (Fig. 1). The L_3 axis of the laboratory system **L** is defined by the scattering vector $\vec{g}_{hkl}$. L_1 and L_2 are the two orthogonal axes lying on the (hkl) plane. If the sample is rotated about the S_1 axis for an angle ψ, then the angle α between L_1 and S_1 is kept constant (Fig. 2). α is the angle between the sample surface and the reflecting planes (hkl) for $\psi = 0°$, i. e. $\alpha = \theta_0 - \gamma$, where θ_0 is the Bragg angle. The strain from the residual stress on the (hkl) plane is defined by

$$\varepsilon_{\alpha\psi} = \varepsilon^{\mathrm{L}}_{33} = \frac{d_{\alpha\psi} - d_0}{d_0}, \qquad (1)$$

where $d_{\alpha\psi}$ and d_0 are the interplanar spacings for the (hkl) plane if $\psi \neq 0°$ and $\psi = 0°$, respectively.

Since we receive the diffraction data in the laboratory system, we have to transform $\varepsilon^{\mathrm{L}}_{33}$ into the strain tensor $\varepsilon^{\mathrm{S}}_{ij}$ given in **S**, according to

$$\varepsilon^{\mathrm{L}}_{33} = A_{3k} A_{3l} \varepsilon^{\mathrm{S}}_{kl}, \qquad (2)$$

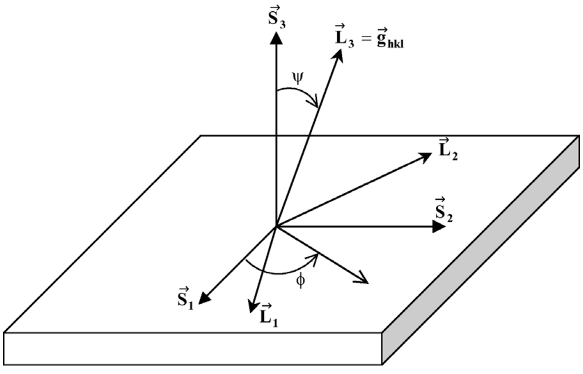

Fig. 1. Definition of the laboratory coordinate system **L**, the sample coordinate system **S**, and the angles ϕ and ψ.

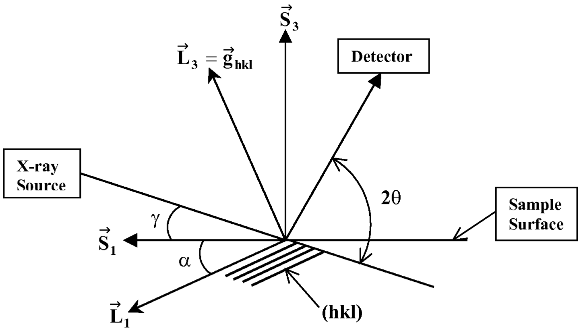

Fig. 2. The laboratory coordinate system **L**, X-ray incident and diffraction directions, and the angle α.

where **A** is the matrix which transforms from **S** to **L**; it is defined by [15]

$$A_{ik} = \begin{bmatrix} \cos\alpha & 0 & -\sin\alpha \\ \sin\alpha\sin\psi & \cos\psi & \cos\alpha\sin\psi \\ \sin\alpha\cos\psi & -\sin\psi & \cos\alpha\cos\psi \end{bmatrix}. \qquad (3)$$

It is evident from (2) and (3) that $\varepsilon^{\mathrm{L}}_{33}$ assumes the following form:

$$\begin{aligned} \varepsilon^{\mathrm{L}}_{33} &= \sin^2\alpha\cos^2\psi\varepsilon_{11} - \sin\alpha\sin 2\psi\varepsilon_{12} \\ &\quad + \sin 2\alpha\cos^2\psi\varepsilon_{13} + \sin^2\psi\varepsilon_{22} \\ &\quad - \sin 2\psi\cos\alpha\varepsilon_{23} + \cos^2\alpha\cos^2\psi\varepsilon_{33}. \end{aligned} \qquad (4)$$

According to the elasticity theory of the residual stress Hooke's law can be formulated as

$$\varepsilon_{ij} = \frac{1+\nu}{E}\sigma_{ij} - \delta_{ij}\frac{\nu}{E}\sigma_{kk}, \qquad (5)$$

where $E = E^{hkl}$ is Young's modulus and $\nu = \nu^{hkl}$ is the Poisson ratio for the polycrystalline film.

With the assumption that shear components are weak ($\sigma_{ij} \cong 0$ for $i \neq j$) and under the hypothesis that the in-plane residual stress is isotropic ($\sigma_{11} = \sigma_{22}$), (4) becomes

$$\begin{aligned} \varepsilon^{\mathrm{L}}_{33} &= \frac{1+\nu}{E}[\sigma_{11} - \sigma_{33}]\cos^2\alpha\sin^2\psi \\ &\quad + \left[\frac{1+\nu}{E}\sin^2\alpha - 2\frac{\nu}{E}\right]\sigma_{11} \\ &\quad + \left[\frac{1}{E}\cos^2\alpha - \frac{\nu}{E}\sin^2\alpha\right]\sigma_{33}. \end{aligned} \qquad (6)$$

Considering residual stress gradient effects, (6) can be written as

$$\varepsilon^{\mathrm{L}}_{33} = \frac{1+\nu}{E}\left[\langle\sigma_{11}\rangle - \langle\sigma_{33}\rangle\right]\cos^2\alpha\sin^2\psi + \left[\frac{1+\nu}{E}\sin^2\alpha - 2\frac{\nu}{E}\right]\langle\sigma_{11}\rangle + \left[\frac{1}{E}\cos^2\alpha - \frac{\nu}{E}\sin^2\alpha\right]\langle\sigma_{33}\rangle. \quad (7)$$

The residual stress profiles $\sigma_{ii}(z)$ along the z-dimension are usually described by polynomial [16] or exponential [17] functions. Assuming that the stress profile has a polynomial behaviour, we write

$$\sigma_{ii}(z) = a_i + b_i z + c_i z^2, \quad i = 1 \text{ or } 3. \quad (8)$$

Because of the exponential attenuation of X-rays in the material, the average stress can be calculated as [16]

$$\langle\sigma_{ii}\rangle = \frac{\int_0^d \sigma_{ii}(z)\mathrm{e}^{-z/\tau}\mathrm{d}z}{\int_0^d \mathrm{e}^{-z/\tau}\mathrm{d}z}, \quad i = 1 \text{ or } 3, \quad (9)$$

where d is the film thickness and τ is the penetration depth of the X-rays.

2.2. X-Ray Penetration in Thin Films under Grazing Incidence

There are several factors which affect the penetration of X-rays inside the specimen: the linear absorption coefficient μ of the material, the incidence angle γ of the X-ray, the Bragg angle θ for the reflection plane (hkl), and the tilt angle ψ of the sample. As we can see from Fig. 3, the path length l of the beam inside the material is given by

$$l = z\left(\frac{1}{\sin(\gamma)} + \frac{1}{\sin(2\theta-\gamma)}\right), \quad (10)$$

where z is the distance below the surface of the sample.

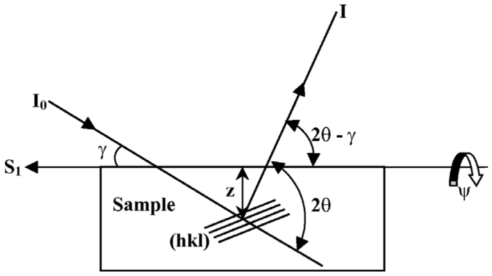

Fig. 3. Absorption of the X-ray beam from the specimen in reflection.

According to the absorption law, the diffracted intensity of the X-ray at a distance z is

$$I = I_0\exp(-\mu l), \quad (11)$$

where I_0 is the primary intensity.

If the sample is rotated about the S_1 axis for an angle ψ (Fig. 1), then the distance z_ψ below the surface is defined by

$$z_\psi = z/\cos\psi, \quad (12)$$

and the diffracted intensity at this distance is

$$I = I_0\exp\left[-\mu\frac{z}{\cos\psi}\left(\frac{1}{\sin(\gamma)} + \frac{1}{\sin(2\theta-\gamma)}\right)\right]. \quad (13)$$

The penetration depth τ is defined as the distance perpendicular to the sample surface, for which the intensity I of the X-ray passing through the material is $1/\mathrm{e}$ of the primary intensity I_0 [18]. The formula for τ is as follows [19]:

$$\tau = \left[\frac{\cos\psi}{\mu}\left(\frac{1}{\sin(\gamma)} + \frac{1}{\sin(2\theta-\gamma)}\right)^{-1}\right] = \frac{\cos\psi(\sin^2\theta - \sin^2\alpha)}{2\mu\sin\theta\sin\alpha}. \quad (14)$$

3. Sample Preparation and Basic Characterizations

3.1. Sample Preparation

Our thin films were deposited in a DC magnetron sputtering system. Prior to film growth the vacuum chamber was evacuated to a pressure of 10^{-7} mbar. Then argon was introduced up to a pressure of 0.01 mbar. The Ag target had a purity better than 99.9%. Before deposition, the targets were presputtered for 5 min with the substrate shutter closed. The substrates were (001)-oriented Si wafers. They were cleaned in an ultrasonic bath and finally sputter-cleaned before deposition.

At first we have prepared a thin silver film, of about 100 nm thickness, to control the deposition parameters and to calibrate the magnetron sputtering equipment. Then, four Ag films of 400 nm thickness were produced at the same time.

3.2. X-Ray Reflectivity Measurements

The density and the thickness of the film has been determined by X-ray reflectivity on a Seifert

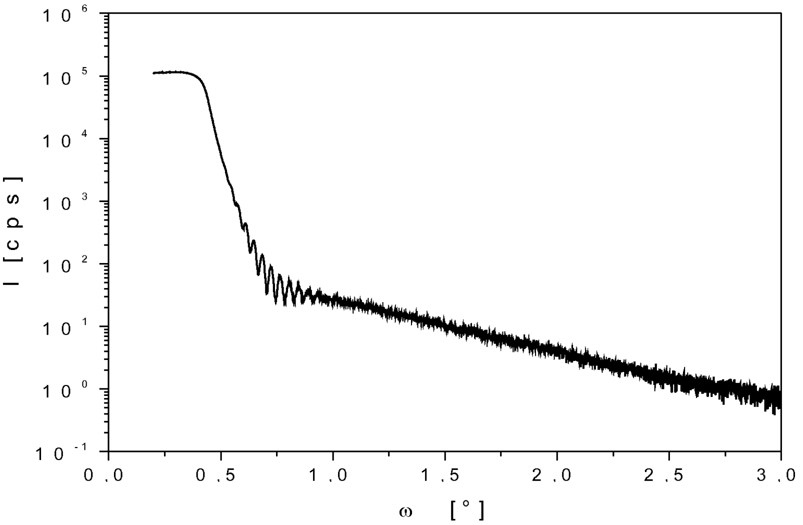

Fig. 4. X-Ray reflectivity measurement of a silver thin film.

PTS 3003 diffractometer using Cu-Kα_1 radiation ($\lambda =$ 0.154056 nm). The incident beam slit width was set to 0.05 mm which gave the best signal resolution. The Cu target was operated at 40 kV with a tube current of 40 mA.

Figure 4 shows the X-ray reflectometry patterns of the first Ag film. Data was analyzed by Analyze, a part of the software system RayfleX (Copyright ©Rich. Seifert & Co). We found that the average density of the first silver film is approximately equal to (10.1 ± 0.2) g/cm^3 and the thickness is about (82 ± 2.5) nm.

4. Surface Acoustic Wave Analysis

An ultrasonic surface wave propagates at the surface of a homogenous material with an amplitude that decreases exponentially perpendicular to the surface and vanishes to negligible values within a few wavelengths below the surface [20]. The penetration depth decreases with increasing frequency. The velocity of propagation is somewhat smaller than the bulk shear velocity associated with the material, which is the same for all frequencies. If the material is coated with a film which has different elastic parameters, the surface wave will become dispersive. Therefore, the wave velocity contains information about the properties of the film.

4.1. Principle of Calculation of the Surface Acoustic Wave Velocity

For thin films grown on substrate, acoustic waves can be excited and propagate in the film or in the substrate. The film acts as a perturbing parameter on the wave propagation velocity. The velocity change depends on the layer thickness, acoustic frequency, and impedance mismatch between layer and substrate.

For an anisotropic linear elastic material with no body force and no piezoelectric effects, the equation for the wave displacement u_i has the form [21]

$$\rho \frac{\partial^2 u_i}{\partial t^2} = \mathbf{C}_{ijkl} \frac{\partial^2 u_k}{\partial x_j \partial x_l}, \quad (i,j,k,l = 1,2,3), \tag{15}$$

where ρ is the density of the medium, $\mathbf{C}_{ijkl}$ is the elastic tensor, and x_i are the coordinates in the sample system **S**.

The particle displacements (u_1, u_2 and u_3) and the traction components caused by the stress components of the wave (T_{13}, T_{23} and T_{33}) must be continuous across the interface under the assumption of a rigid contact between the two materials (film and substrate). Since the free surface is considered to be mechanically stress-free, the three traction components of stress must vanish thereon and nine boundary conditions are obtained. In order to obtain nontrivial solutions of this set of homogenous equations, the 9.9 determinant must vanish [20]. Consequently, the following equation is obtained:

$$\begin{aligned} &F(f,h,V_{\mathrm{Rg}},E,E',\nu,\nu',\rho,\rho') \equiv |a_{ij}| = 0 \\ &(i,j = 1,2,\ldots,9). \end{aligned} \tag{16}$$

Here f is the excitation frequency, V_{Rg} is the guessed Rayleigh wave phase velocity, (E,ν,ρ) and (E',ν',ρ')

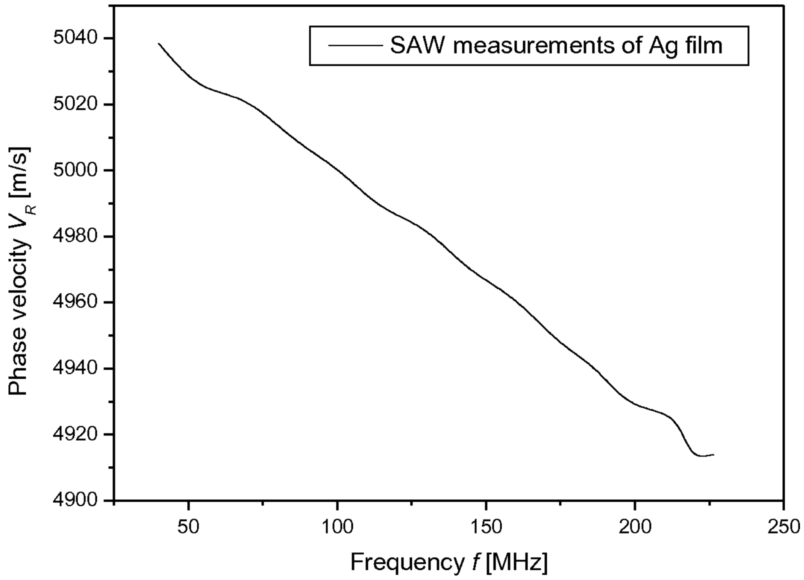

Fig. 5. Experimental dispersion curve of the first Rayleigh waves propagating in Ag/Si(001).

are Young's modulus, the Poisson ratio, and the density of the film and the substrate, respectively, h is the film thickness, and a_{ij} are the components of the boundary-condition determinant. Details on F and the a_{ij} can be found in [20, 21].

4.2. Experimental Determination of the Dispersion Curve

Laser acoustic wave measurements are a nondestructive method for the characterization of elastic properties of thin films. The laser ultrasonic experimental equipment utilized for this study has been developed in the Fraunhofer-Institut for Material and Beam Technology, Dresden, Germany [22]. Short pulses (pulse duration, 0.5 ns; energy, 0.4 mJ) of a nitrogen laser are focused by a cylindrical lens on the surface of the sample and generate wide-band surface wave pulses. These pulses are detected by a wide-band piezoelectric transducer (bandwidth, 250 MHz). Specimen and transducer are fixed to a translation stage that moves perpendicular to the position of the laser beam to vary the distance d between the laser focus line and the transducer. The surface acoustic waveform is detected at different distances d_1 and d_2. A Fourier transform of the waveform yields the phase spectra $\phi_1(f)$ and $\phi_2(f)$. The Rayleigh wave velocity V_R depending on the frequency f is determined according to [22]

$$V_R(f) = \frac{2\pi f(d_2 - d_1)}{\phi_2(f) - \phi_1(f)}. \tag{17}$$

The measured dispersion relation for the first Rayleigh mode propagating in the Ag/Si(001) system is shown in Figure 5.

4.3. Determination of Young's Modulus and the Poisson Ratio of the Ag Film

As we can seen from (16), that the function F depends on seven unknown parameters. Young's modulus E', the Poisson ratio ν', and the density ρ' of the substrate Si were obtained from literature. The values of h and ρ were determined from X-ray reflectometry measurements. Young's modulus E and the Poisson ratio ν of the Ag film were the unknown parameters.

An error function which defines the difference between the measured (V_R) and the guessed (V_{Rg}) phase velocities was defined as

$$e = \frac{\sum_{i=1}^{N} [V_R(i) - V_{Rg}(i)]^2}{\sum_{i=1}^{N} [V_R(i)]^2}, \tag{18}$$

where i represents the discrete nondimensional wave number and N is the number of data points.

An initial guess of E and ν was made first, then the forward computer program for calculating the phase velocity dispersion of surface acoustic waves was utilized to calculate the guessed phase velocity V_{Rg} according to (16). The value of the error function could thus be obtained from (18). The true Young's modulus

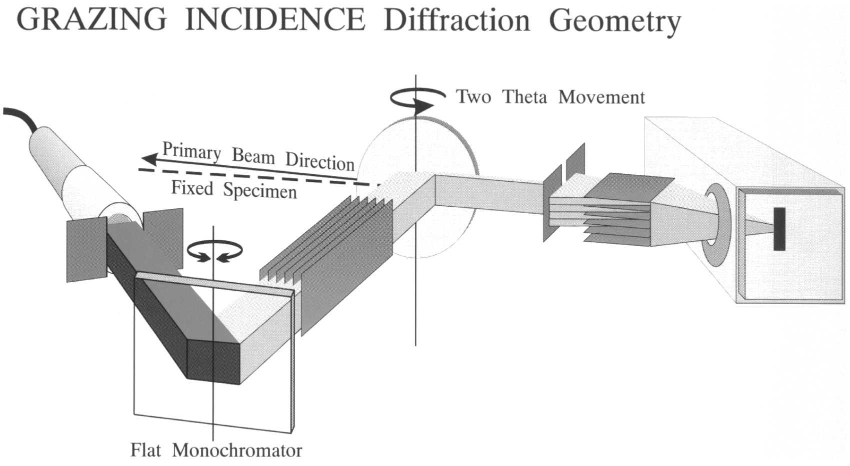

Fig. 6. The diffraction geometry of the Seifert PTS 3003 Bragg-Brentano diffractometer in GIXD mode (picture reproduced by courtesy of Seifert).

E and the Poisson ratio ν of the film were then determined using the simplex method [21].

The measured dispersion relation for the first Rayleigh mode propagating in the Ag/Si(001) system shown in Fig. 5 was utilized to determine inversely Young's modulus E and the Poisson ratio ν of the Ag film. Data analysis was done using LA-wave software. The refined results are $E = (83 \pm 1.2)$ GPa and $\nu = (0.3 \pm 0.002)$.

5. X-Ray Diffraction Measurement

5.1. Conversion of the Conventional Diffractometer

As already outlined, the strain-stress analysis of the samples has been carried out using X-ray diffraction (XRD). We had a four-circle powder diffractometer Seifert PTS 3003 at our disposal. The diffractometer was equipped with a Cu tube. The operation voltage and current were 40 kV and 40 mA, respectively.

The conversion of our conventional powder diffractometer into a grazing incidence diffractometer was accomplished by mounting a long Soller slit on the detector side with its plates perpendicular to the diffraction plane. The entire configuration consisted of a primary divergence slit (1 mm), an axial Soller slit to limit axial divergence on the primary (tube) side, a secondary divergence slit (0.3 mm), and the mentioned long Soller slit (0.4°) on the secondary side. A flat graphite monochromator was placed in front of the scintillation counter. The radius R_d was 360 mm which is fairly large for a conventional diffractometer and provides good angular resolution (Fig. 6).

5.2. Lattice Spacing Depth Profiling

The above outlined ABG method has been applied to several Ag films of 400 nm thickness. For GIXD, the angle γ between the incident X-ray beam and the sample surface was kept constant at $\gamma = 3^\circ$. For this incidence angle the X-ray could penetrate through the depth of the Ag films. The detector scanned in the 2θ range from 33° to 42° to measure the Ag(111) peak ($2\theta_0 = 38.11^\circ$). The (111) plane was used due to its relatively strong intensity. The goniometer error function $G(\theta, \psi, \gamma)$ for the GIXD geometry has been measured using polycrystalline standard Ag samples. All measured reflection positions θ were corrected using $G(\theta, \psi, \gamma)$. Four samples were studied. At first, the X-ray stress measurements were applied to the samples as deposited. Subsequently, the films were annealed at selected temperatures in a sealed glass tube under argon gas for 90 min with a heating step of 5 °C/min. The temperature range was from $T = 100$ °C to 700 °C in steps of $\Delta T = 200$ °C. The experimental results of the lattice spacing vs. $\cos^2\alpha \sin^2\psi$ plot of Ag(111) reflection are shown in Fig. 7 as solid squares. A nonlinearity variation has been found. It can be attributed to the presence of a residual stress gradient in the samples.

6. Stress Depth Profile Evaluation

6.1. Basic Relations

Working out the integral, (8) becomes

$$\langle \sigma_{ii} \rangle = a_i + b_i \left(\tau + \frac{d}{1 - \mathrm{e}^{d/\tau}} \right) + c_i \left(2\tau^2 + \frac{d(d + 2\tau)}{1 - \mathrm{e}^{d/\tau}} \right), \quad i = 1 \text{ or } 3. \tag{19}$$

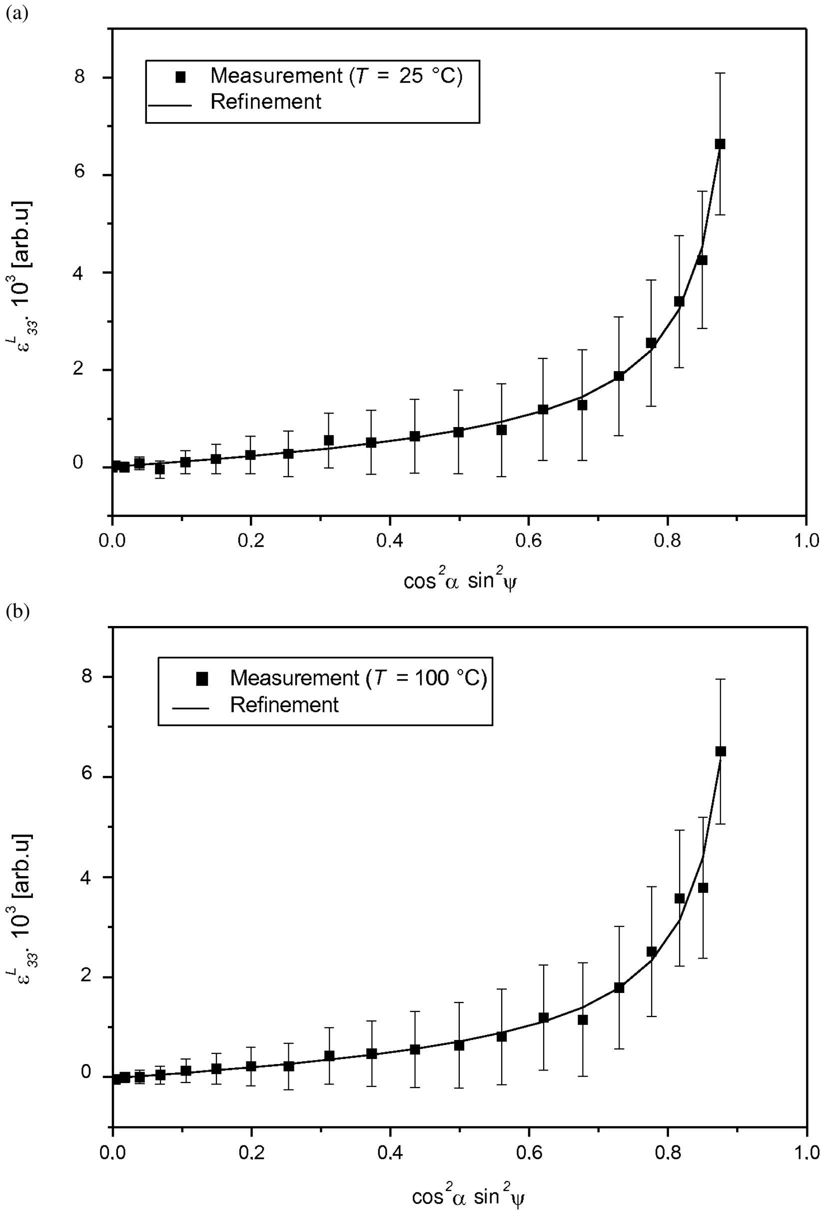

Fig. 7. Residual strain versus $\cos^2\alpha\sin^2\psi$ for (111) reflections. The solid squares are the experimental results and the solid line is the model. (a) Sputtered Ag film; (b) annealed Ag film at 100 °C; (c) annealed Ag film at 300 °C; (d) annealed Ag film at 500 °C; (e) annealed Ag film at 700 °C; (f) all Ag films.

The equilibrium conditions of the linear elasticity theory

$$\nabla\sigma_{ij} = 0, \quad i,j = 1,2,3, \tag{20}$$

and the surface boundary conditions

$$\sigma_{i3}(z = 0) = 0, \quad i = 1,2,3, \tag{21}$$

must be used for the resolution of the depth-dependent stress state [16]. Equation (11) imposes that all forces in the body must be in equilibrium. Equation (21) reflects that all components of the stress on the free sample surface must vanish. Taking into account the conditions imposed by (20) and (21) the coefficients a_3 and b_3 must vanish.

6.2. Residual Stress Gradients of Annealed Ag Polycrystalline Thin Films

From (14) and by refining (7) and (19) to the data of Fig. 7 using nonlinear least-squares modelling, the

(c)

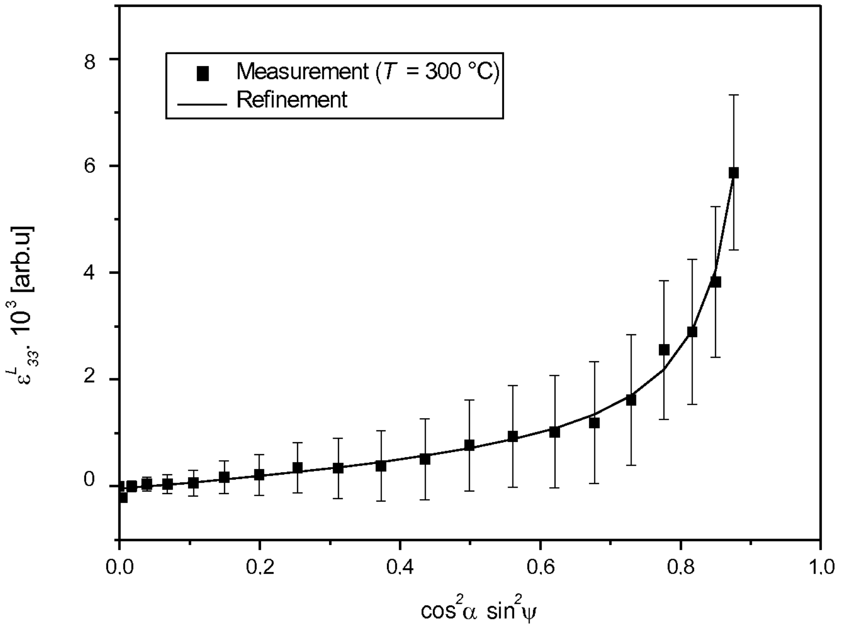

(d)

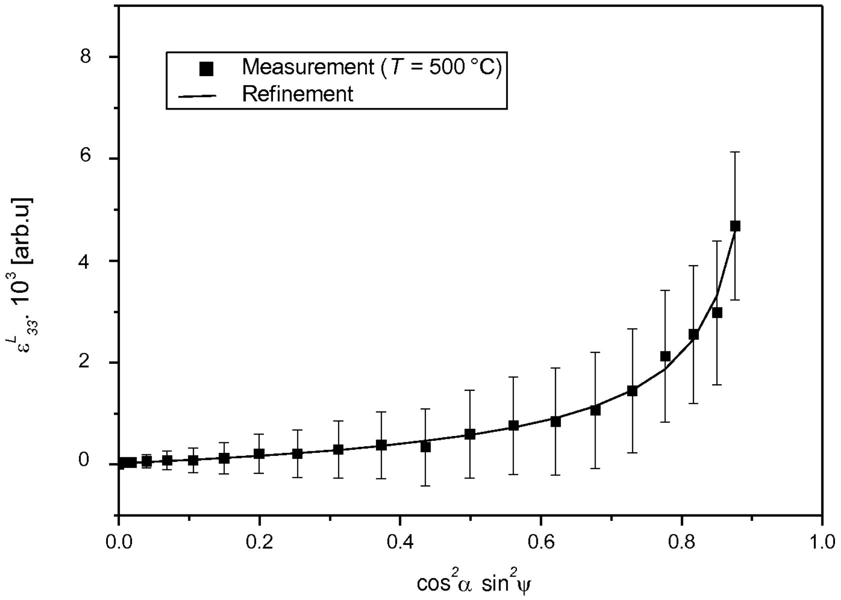

Fig. 7 (continued).

refining parameters a_i, b_i and c_i ($i = 1$ or 3) will be obtained.

The refined $\cos^2\alpha\sin^2\psi$ data plots considering the residual stress gradient effect are shown in Fig. 7 as full lines. Table 1 presents the obtained refining parameters for different data plots.

The corresponding stress components [$\sigma_{11}(z) = \sigma_{22}(z)$ and $\sigma_{33}(z)$] as functions of the position below the surface [cf. (8)] are shown in Fig. 8 and Fig. 9 for Ag films annealed at different temperatures.

For our thin films no phase transition phenomena occurred and epitaxial stresses played no role. So, the total residual stress presented in the Ag films was a combination of the intrinsic stresses (σ_{in}) and the thermal stresses (σ_{th}).

(e)

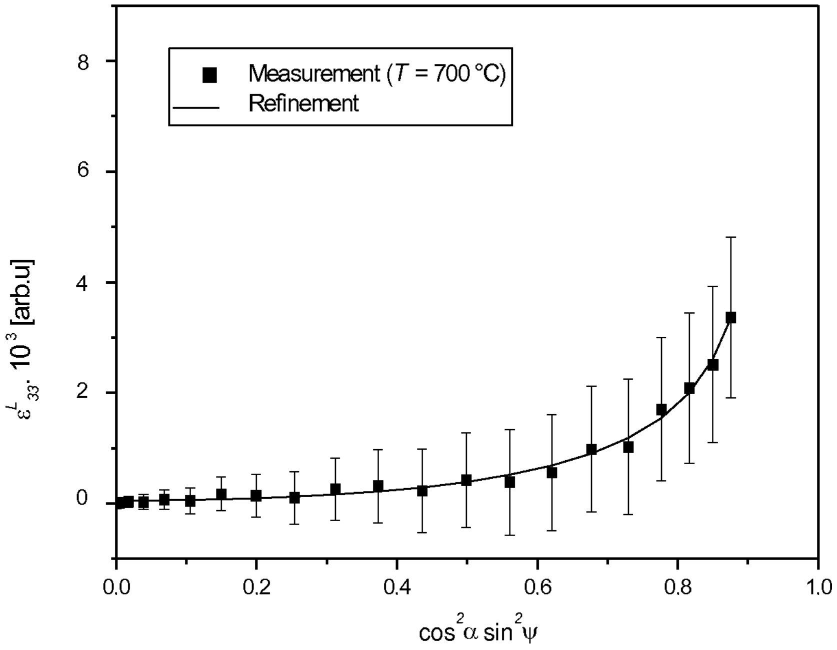

(f)

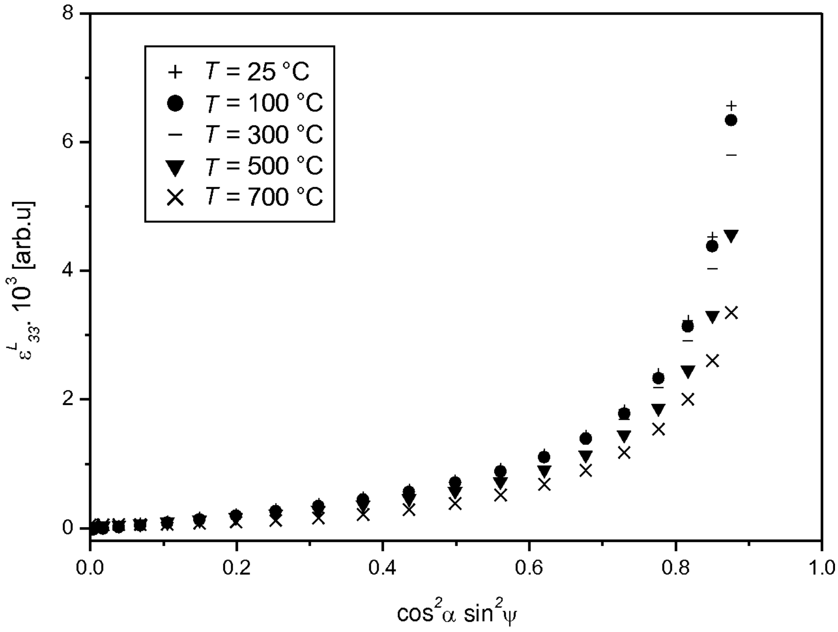

Fig. 7 (continued).

Figure 8 shows the in-plane stress (σ_{11} and σ_{22}) trends as functions of the position below the sample surface. The in-plane components of the residual stress in Ag films at the top are between -1 GPa and -9 GPa and increase with the distance from the surface. At a depth between 210 nm and 275 nm, a change to tensile stress is seen. Thermal stress increases with the annealing temperature, so the tensile stress components σ_{11} and σ_{22} increase at the interface with temperature and reach a maximum of about 10 GPa for the sample annealed at 700 °C.

T [°C]	a_1 [GPa]	b_1 [GPa/nm]	c_1 [GPa/nm^2]	c_3 [GPa/nm^2]
25	-9.04 ± 1.05	$(4.40\pm0.20)\cdot10^{-2}$	$(-2.86\pm0.50)\cdot10^{-5}$	$(-2.37\pm0.20)\cdot10^{-6}$
100	-8.50 ± 1.80	$(3.60\pm0.33)\cdot10^{-2}$	$(-1.53\pm0.25)\cdot10^{-5}$	$(-2.22\pm0.34)\cdot10^{-6}$
300	-7.90 ± 1.13	$(3.61\pm0.28)\cdot10^{-2}$	$(-2.26\pm0.60)\cdot10^{-5}$	$(-2.17\pm0.24)\cdot10^{-6}$
500	-4.49 ± 1.03	$(4.25\pm0.19)\cdot10^{-2}$	$(5.98\pm0.90)\cdot10^{-5}$	$(-1.78\pm0.19)\cdot10^{-6}$
700	-0.90 ± 0.08	$(-2.3\pm0.15)\cdot10^{-2}$	$(13.10\pm2.05)\cdot10^{-5}$	$(-1.04\pm0.15)\cdot10^{-6}$

Table 1. The refined a_1, b_1, c_1 and c_3 coefficients for all Ag films annealed at different temperatures.

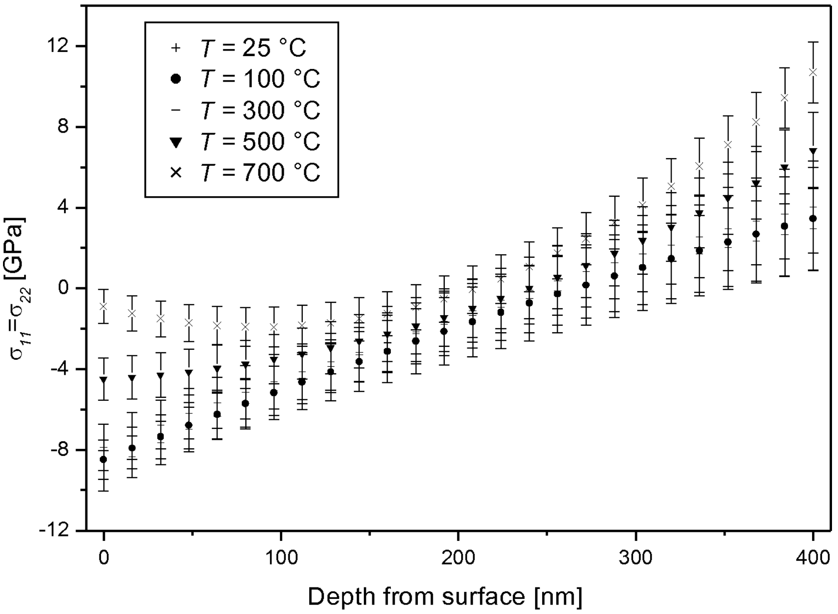

Fig. 8. Refined in-plane residual stress. Profile of post-annealing Ag films.

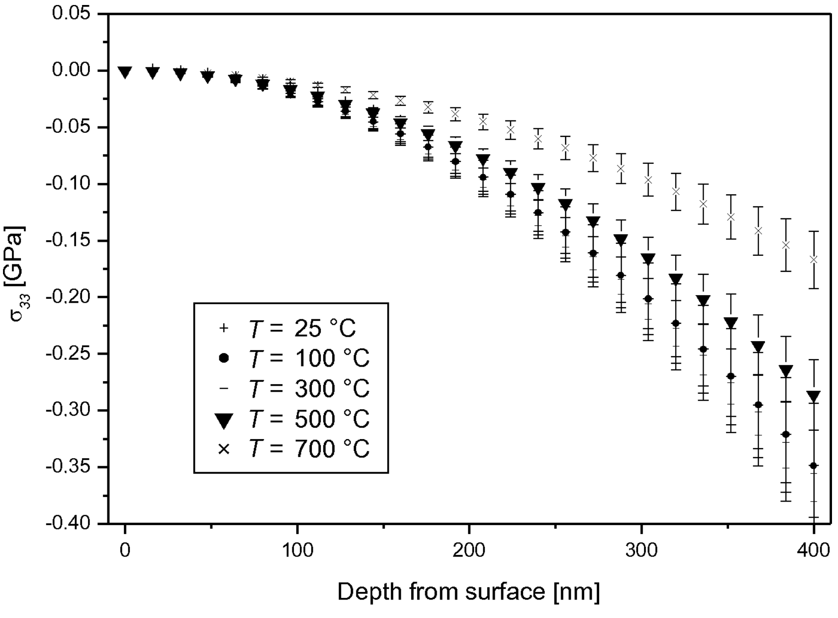

Fig. 9. Refined out-of-plane residual stress. Profile of post-annealing Ag films.

Figure 9 shows a compressive out-of-plane component (σ_{33}). At the sample surface, σ_{33} is close to zero, which satisfies (21), and increases with the depth from the surface sample. Generally, the out-of-plane residual stress is assumed to be zero, but in our case it is invalid (Fig. 9). Our results show that the in-plane component of the residual stress is larger than the out-of-plane component for all Ag films, but the out-of-plane component is not that small to be neglected. The maximum of the component σ_{33} at the sample interface is of about -0.35 GPa for the deposited Ag film. For weak-textured and isotropic films, the out-of-plane residual stress could be neglected. But in our case, the out-of-plane residual stress must be considered. One can conclude that during the formation of texture in Ag layers, as the texture becomes stronger, the residual stress becomes larger. For the sample annealed at 700 °C the out-of-plane residual stress decreases and reaches -0.15 GPa which shows the effect of the temperature on the texture formation and residual stress behaviour.

7. Conclusions

Four Ag thin films, of 400 nm thick, were prepared by c-magnetron sputtering on Si(001) substrates. The average density of the polycrystalline silver materials ($\rho = 10.1$ g/cm^3) was determined by reflectinity measurements. Laser acoustic wave measurements were applied to determine Young's modulus ($E = 83$ GPa) and the Poisson ratio ($\nu = 0.3$) of the films. The films were annealed at different temperatures (100 °C, 300 °C, 500 °C, and 700 °C). Grazing incidence X-ray diffraction measurements were used for residual stress evaluation utilizing the (111) plane reflection. Nonlinearity was found in the $\cos^2\alpha \sin^2\psi$ plots. By application of the differential equation of equilibrium and the surface boundary conditions for every stress tensor component σ_{ii}, a model function $\sigma_{ii}(z)$ was extracted. The data were fitted and the residual stress trends along the film depth were obtained. The stress gradients were found to be sensitive to the annealing process.

Compressive out-of-plane stresses (σ_{33}) in our Ag films were found which prove the formation of texture in Ag films. The out-of-plane residual stresses were equal to zero near the free surface of the films and increased from top to bottom. The maximum, reached at the interface, decreased with increasing annealing temperature. The in-plane stresses (σ_{11} and σ_{22}) were compressive in a depth range between 210 nm and 275 nm from the samples surface. After reaching a value of zero they increased to high-tensile values. The maximum, reached at the interface, increased with elevated post-annealing temperature which proves the dominance of thermal stresses near the substrate.

Acknowledgements

A. Njeh is grateful to the Minister of High Education of Tunisia and to the German Foreign Exchange Service (DAAD). M. H. Ben Ghozlen is grateful to the Alexander von Humboldt foundation for financial support. Many thanks to Dr. Thomas Wieder for discussions on the manuscript.

[1] S. Y. Kweon, S. H. Yi, and S. K. Choi, J. Vac. Sci. Technol. A **15**, 57 (1997).
[2] W. D. Nix, Metall. Trans. A **20**, 2217 (1989).
[3] H. P. Klug and L. E. Alexander, X-Ray Diffraction Procedures, Wiley, New York 1974.
[4] R. Glockner, Z. Tech. Phys. **15**, 421 (1934).
[5] E. Macherauch and P. Müller, Z. Phys. **13**, 305 (1961).
[6] I. C. Noyan and J. B. Cohen, Residual Stress, Measurement by Diffraction and Interpretation, Springer-Verlag, New York 1987.
[7] P. H. Fuoss and S. Brennan, Ann. Rev. Mater. Sci. **20**, 365 (1990).
[8] A. Njeh, T. Wieder, and H. Fuess, Powder Diffraction **15**, 211 (2000).
[9] S. G. Malhotra, Z. U. Rek, S. M. Yalisove, and J. C. Bilello, J. Appl. Phys. **79**, 6872 (1996).
[10] A. Segmüller and M. Murakami, Characterization of Thin Films by X-Ray Diffraction, Academic Press, USA 1985.
[11] K. Van Acker, L. De Buyser, J. P. Celis, and P. Van Houtte, J. Appl. Cryst. **27**, 56 (1994).
[12] J. Zendehroud, T. Wieder, K. Thoma, and H. Gärtner, Haerterei-Tech. Mitt. **48**, 41 (1993).
[13] J. Zendehroud, T. Wieder, and H. Klein, Materialwiss. Werkstofftechnik **26**, 553 (1995).
[14] T. Wieder, Thin Solid Films **256**, 39 (1995).
[15] C.-H. Ma, J.-H. Huang, and H. Chen, Thin Solid Films **418**, 73 (2002).
[16] M. Härting, Acta Mater. **46**, 1427 (1998).
[17] V. Hauk and W. K. Krug, Haerterei-Tech. Mitt. **43**, 164 (1988).
[18] C. Genzel, Mat. Sci. Technol. **21**, 10 (2005).
[19] M. J. Marques, A. M. Dias, P. Gergaud, and J. L. Lebrun, Mat. Sci. Eng. A **287**, 78 (2000).
[20] G. W. Farnell and E. L. Adler, Phys. Acoust. **9**, 35 (1972).
[21] A. Njeh, N. Abdelmoula, H. Fuess, and M. H. Ben Ghozlen, Z. Naturforsch. **60a**, 789 (2005).
[22] D. Schneider and T. Schwarz, Surf. Coat. Technol. **91**, 136 (1997).